Electronic Supplementary Information – Twofold Rattling Mode Induced Ultralow Thermal Conductivity in Vacancy-Ordered Double Perovskite Cs_2SnI_6

Un-Gi Jong[1]*, Yun-Sim Kim[1], Chol-Hyok Ri[1], Yun-Hyok Kye[1], Chol-Jin Pak[1], Stefaan Cottenier[2], Chol-Jun Yu[1]†

[1] *Computational Materials Design (CMD), Faculty of Materials Science, Kim Il Sung University, Ryongnam-Dong, Taesong District, Pyongyang, Democratic People's Republic of Korea.*

[2] *Department of Electromechanical, Systems and Metal Engineering & Center for Molecular Modeling (CMM), Ghent University, Technologiepark-Zwijnaarde 46, BE-9052 Ghent, Belgium.*

February 7, 2022

Computational details

Our first-principles calculations were performed using the VASP code [1, 2], employing the projector augmented wave potentials [3, 4] with the valence electron configurations of Cs–$5s^25p^66s^1$, I–$5s^25p^5$ and Sn–$5s^25p^2$. We utilized the PBEsol functional [5] known to accurately predict the lattice constants of all-inorganic HPs [13], being crucial for a reliable description of lattice dynamics. We used a kinetic energy cutoff of 800 eV for a plane-wave basis and a k-point mesh of 12×12×12 for Brillouin zone (BZ) integrations, which are enough to guarantee a total energy accuracy as 5 meV/cell. Lattice dynamics and thermal conductivity calculations were performed using the ALAMODE code [8, 9, 14]. Full details of our calculations with supercell-size convergence tests for the phonon calculations is provided in the Supplementary Material. The atomic positions were relaxed until the atomic forces are smaller than 10^{-3} eV/Å, while the energy convergence criterion was set to be 10^{-8} eV. The optimized lattice constants are 6.18 and 11.62 Å for $CsSnI_3$ with cubic $Pm\bar{3}m$ space group and Cs_2SnI_6 with cubic $Fm\bar{3}m$ space group, which are in close agreement with the experimental values of 6.22 and 11.65 Å [6, 7]. The harmonic interatomic force constants (IFCs) were extracted using a $3 \times 3 \times 3$ supercell expansion and a displacement step of 0.01 Å, while the anharmonic IFCs were computed using $2 \times 2 \times 2$ supercell expansion. For 3×3×3 supercell calculations, we used the same convergence thresholds with a reduced kinetic energy cutoff of 400 eV and 3×3×3 k-point mesh.

In order to calculate the harmonic phonon eigenvalues and phonon DOS, we used the second-order (harmonic) IFCs by utilizing the finite displacement method with 3×3×3 supercell, as implemented in the ALAMODE code [8, 9]. Then, we calculated the atomic forces for each displaced configurations and extracted harmonic IFCs by using the ALAMODE code. We performed the convergence tests of the phonon eigenvalues with respect to the supercell size, revealing that the results of 2×2×2 supercell agree well with the ones of 4×4×4 (3×3×3) supercell for $CsSnI_3$ (Cs_2SnI_6) as shown in Fig. S2. We employed even dimensioned supercell that spans commensurate q-point grids in order to check for cell size convergence in $CsSnI_3$ [12].

We performed self-consistent phonon (SCP) calculations including cubic and quartic anharmonicities at finite temperatures by using up to sixth-order IFCs. [8, 9]. Within the SCP theory, the anharmonic phonon eigenvalues were computed as functions of temperature from the pole of the Green's function beyond the perturbation theory, as implemented in the ALAMODE code. In the SCP equation, the phonon self-energy becomes frequency-dependent only treating the loop diagram related with the quartic IFCs. Note that the off-diagonal elements of the self-energy should be accounted to allow the phonon eigenvectors to change by anharmonic effects [9]. The current SCP approach applied to this work was confirmed to be efficient and accurate in accounting for lattice dynamics and thermal transport properties of systems with severe anharmonicity. For estimating anharmonic IFCs, we employed the compressive sensing lattice dynamics (CSLD) approach [10], as implemented in the ALAMODE code. To do this, we prepared over 60 configurations where all of the atoms are displaced randomly with large displacements [10] and computed atomic forces for each configuration using precise DFT calculations. We employed the method suggested by F. Zhou[10] for generating structures with large random displacement. The atomic displacements $\boldsymbol{u}$ can be generated according to a given covariance matrix $\Sigma(\boldsymbol{u})$. To proceed, a lower triangle matrix L needs to be computed through Cholesky decomposition of Σ, i.e., $LL^T = \Sigma(\boldsymbol{u})$. Provided that a vector $\boldsymbol{x}$ with the same dimension of $\boldsymbol{u}$ has a covariance matrix of $\Sigma(\boldsymbol{x})$ and the variance of $\boldsymbol{u} \equiv L\boldsymbol{x}$ is $\bar{L}(\boldsymbol{x})$, the covariance of $L\boldsymbol{x}$ becomes $L\Sigma(\boldsymbol{u})L^T$. Therefore, $\Sigma(\boldsymbol{u})$ can be recovered if $\boldsymbol{x}$ has identity covariance matrix, indicating that $\boldsymbol{u}$ can be generated using $\boldsymbol{x}$ that follows the Gaussian

*Corresponding author: Un-Gi Jong, Email: ug.jong@ryongnamsan.edu.kp
†Corresponding author: Chol-Jun Yu, Email: cj.yu@ryongnamsan.edu.kp

distribution. According to this scheme as implemented in CSLD code [10], we generated 60 configurations with large random displacements with maximum displacement of 0.81 Å and minimum displacement of 0.07 Å. For cubic and quartic IFCs, we included up to 5th- and 3rd-nearest neighbor shells, whereas fifth- and sixth-order IFCs were considered for nearest-neighbor pairs. In order to estimate the accuracy of the IFCs estimated by the CSLD, we calculated potential energy ($U-U_0$) and atomic forces by using the atomic displacements and the IFCs for Cs_2SnI_6. Fig. S9 shows the comparison of the potential energy and the atomic forces obtained from DFT and IFCs. The relative errors were 1.2 and 5.6 % for the potential energy and the atomic force, respectively. On the other hand, the model in this work can reproduce the double well potential with the well-depth of about 40.2 meV, which is in good agreement with our previous calculations [13].

With the calculated 3rd-order IFCs, we solved the Boltzmann transport equation (BTE) for phonon within the relaxation time approximation (RTA) and estimated the lattice thermal conductivity, as implemented in the ALAMODE code. We performed convergence test for the calculations of lattice thermal conductivity κ according to the size of q-point mesh in the phonon BZ, demonstrating that a 24×24×24 q-point mesh is sufficient to determine κ with an error less than 0.01 W/m·K (Fig. S3). In this work, we considered diagonal contributions [11] only by solving the BTE equation and ignored thermal expansion of the crystal volume at high temperatures but the κ_l calculated with and without the SCP eigenvalues are in reasonable agreement with the experimental values [6] for the cubic $CsSnI_3$, convincing that our calculations can provide reliable results. With reference to calculation method of the lattice thermal conductivity κ_l, BTE corresponds to the κ_l calculated by using the harmonic phonon dispersions at 0 K without any anharmonic effects while BTE+SCP stands for the κ_l estimated by using the anharmonic phonon dispersions obtained at finite temperatures within the SCP theory.

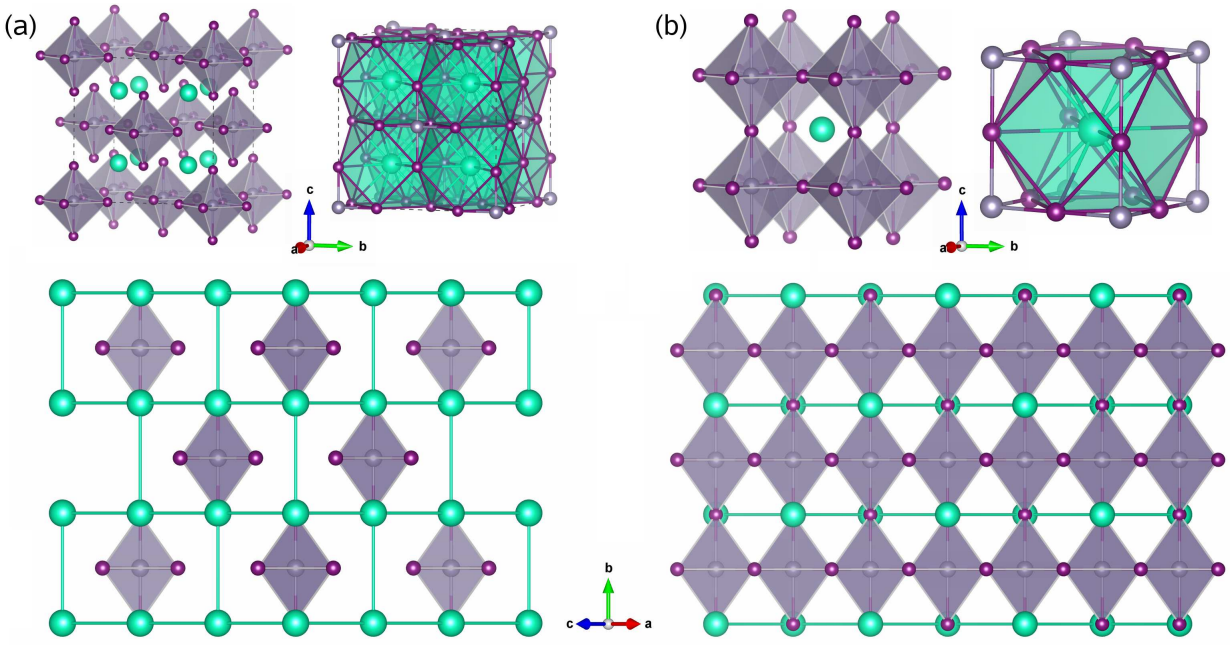

Fig. S1. Polyhedral view of crystalline structure (top-left), local coordination environments of Cs atoms-rattler inside a cub-octahedral cage formed by I atoms (top-right), and isolated and corner-sharing SnI_6 octahedra clusters-rattler inside cage-like structures composed of Cs atoms (bottom) in (a) vacancy-ordered double tin iodide perovskite Cs_2SnI_6 with cubic $Fm\bar{3}m$ space group and (b) single tin iodide perovskite $CsSnI_3$ with cubic $Pm\bar{3}m$ space group. Green-, gray-, and purple-colored balls represent Cs, Sn, and I atoms, respectively.

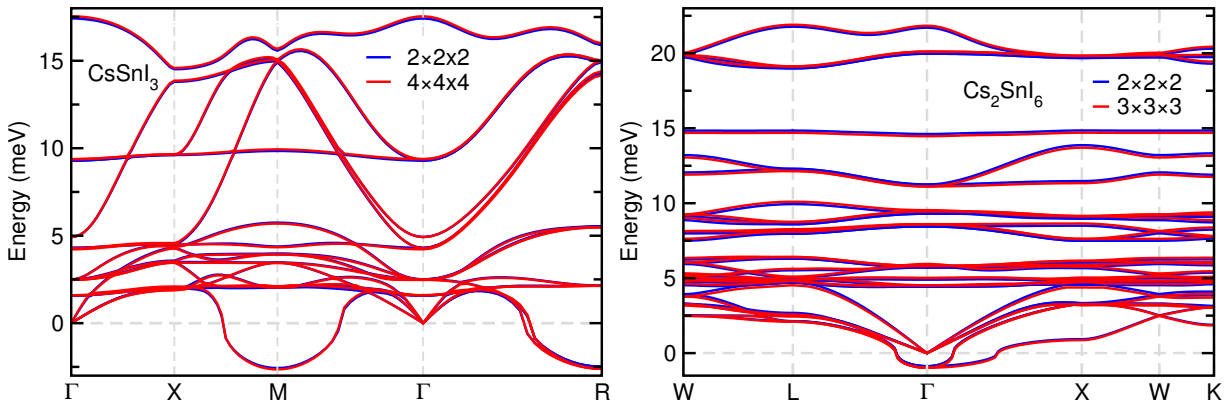

Fig. S2. Comparison of harmonic phonon dispersions calculated using 2×2×2 and 4×4×4 (3×3×3) supercells of cubic $CsSnI_3$ (Cs_2SnI_6) at 0 K, respectively.

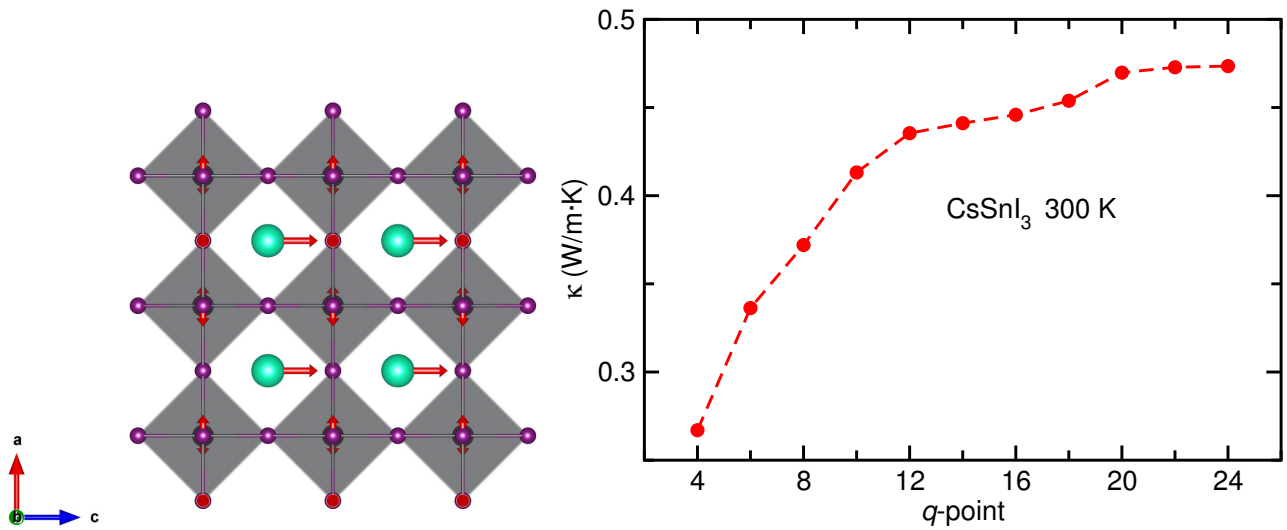

Fig. S3. Polyhedral view of collective motion of atoms in $CsSnI_3$, corresponding to the lowest optical mode at Γ point, and lattice thermal conductivity as a function of q-point mesh for $CsSnI_3$.

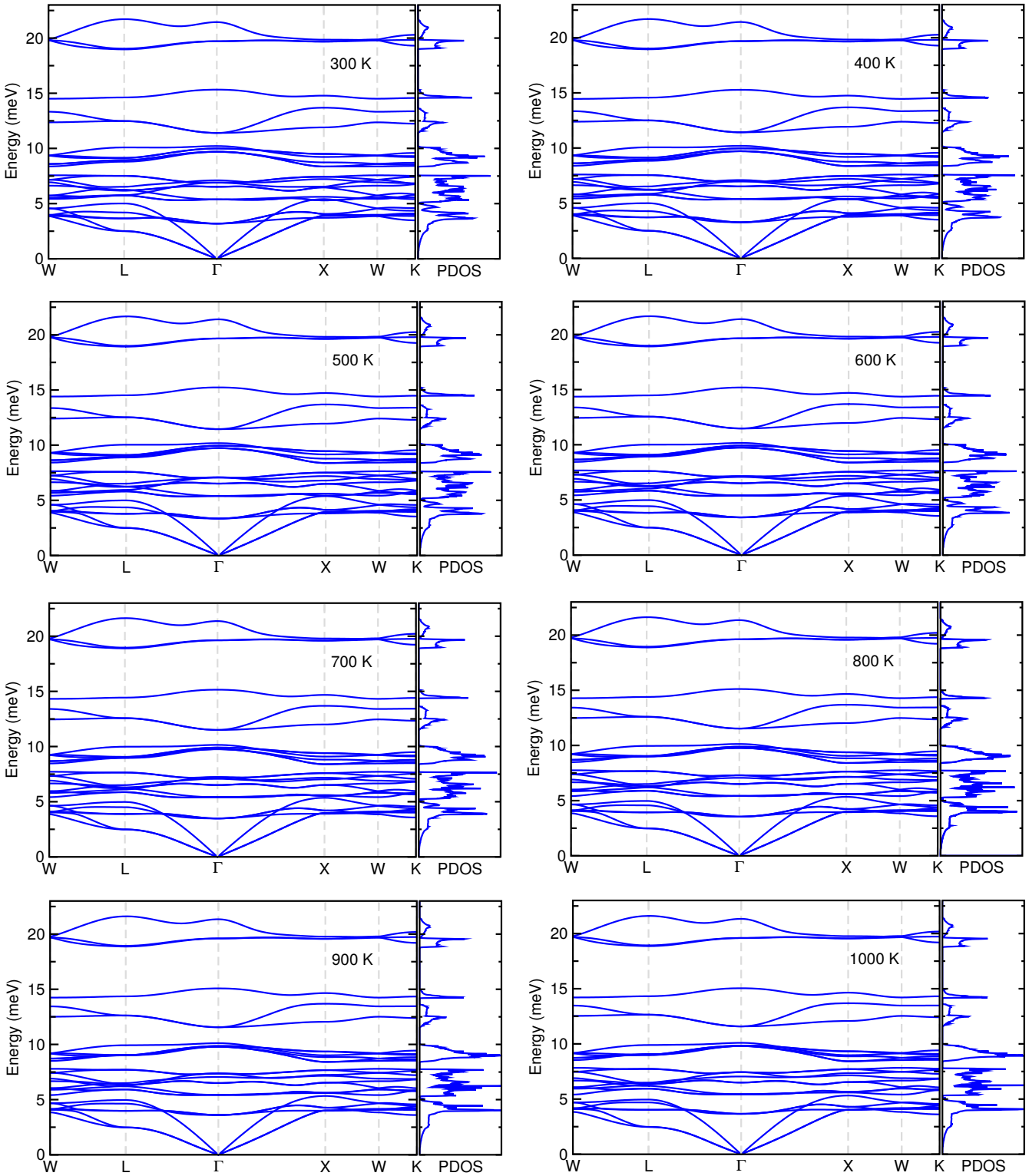

Fig. S4. Temperature-dependent anharmonic phonon dispersion curves with phonon DOS for Cs_2SnI_6 at temperatures from 300 to 1000 K with an interval of 100 K.

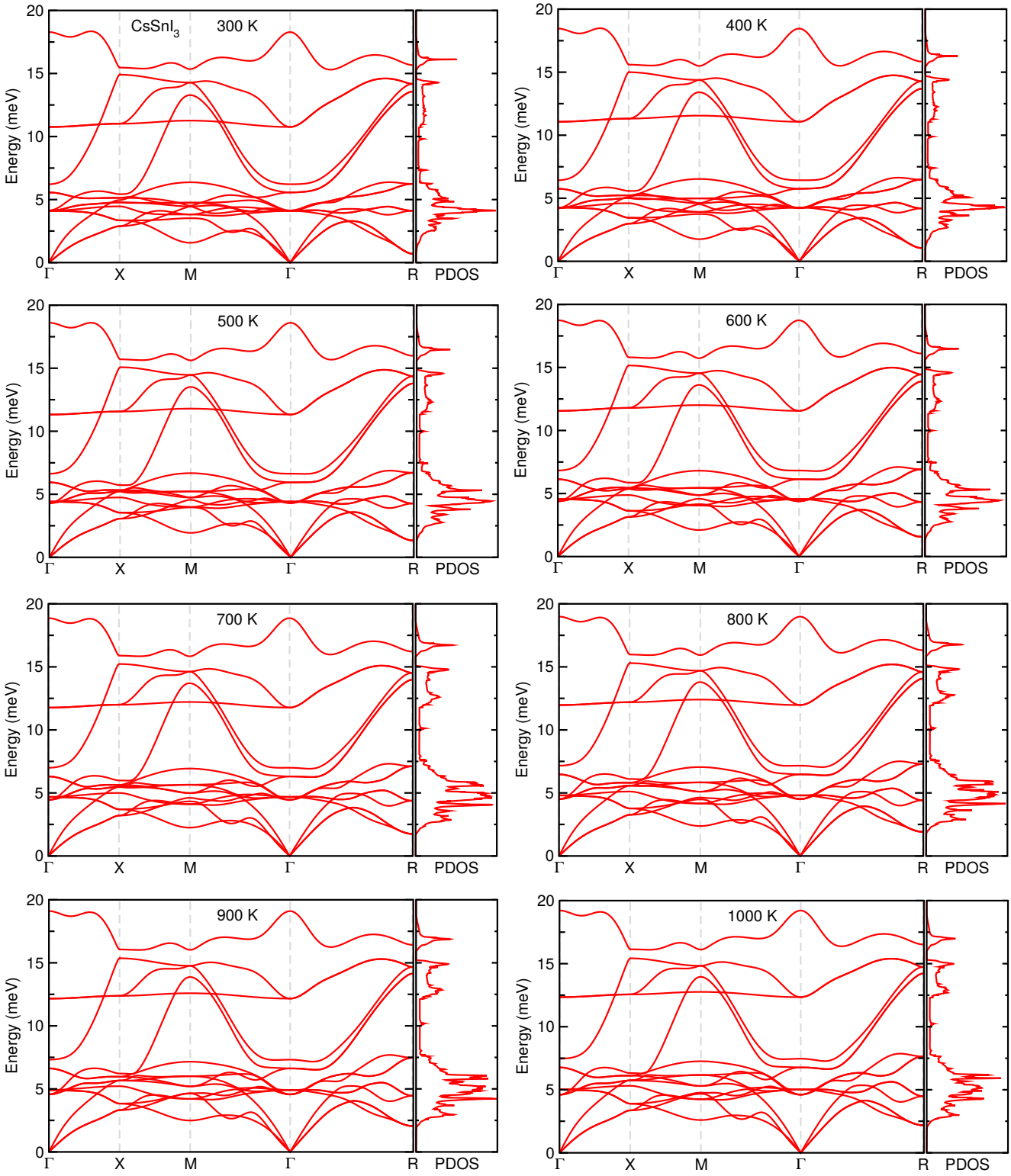

Fig. S5. Temperature-dependent anharmonic phonon dispersion curves with phonon DOS for $CsSnI_3$ at temperatures from 300 to 1000 K with an interval of 100 K.

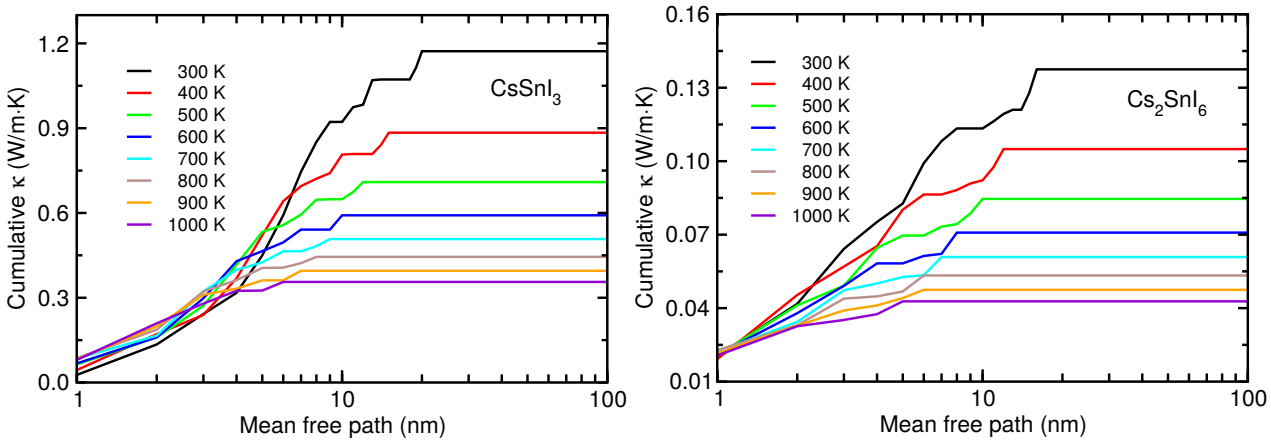

Fig. S6. Cumulative thermal conductivity calculated with BTE+SCP method for $CsSnI_3$ and Cs_2SnI_6.

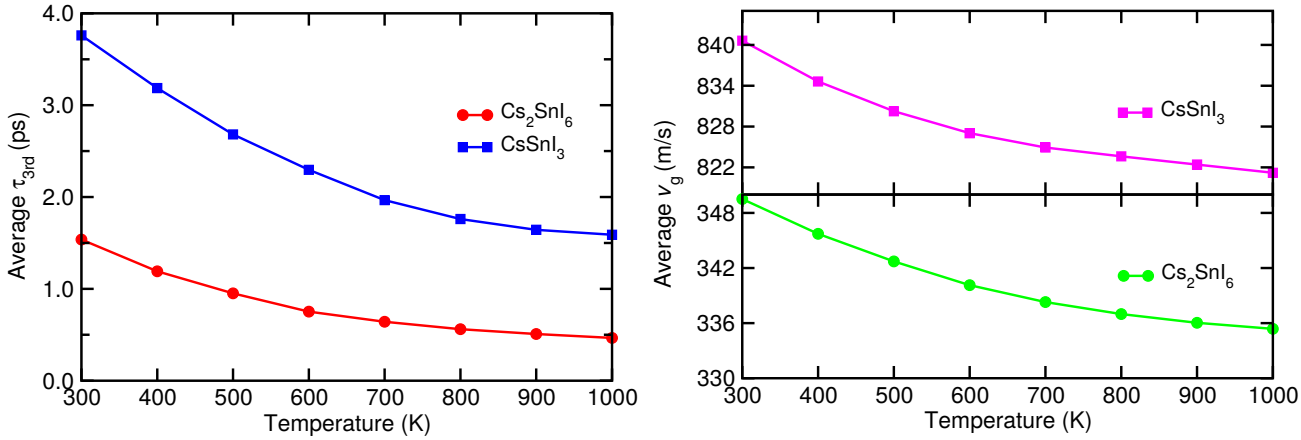

Fig. S7. Average phonon lifetime τ_{3rd} and group velocity v_g at temperatures from 300 to 1000 K with an interval of 100 K calculated with BTE+SCP method for $CsSnI_3$ and Cs_2SnI_6.

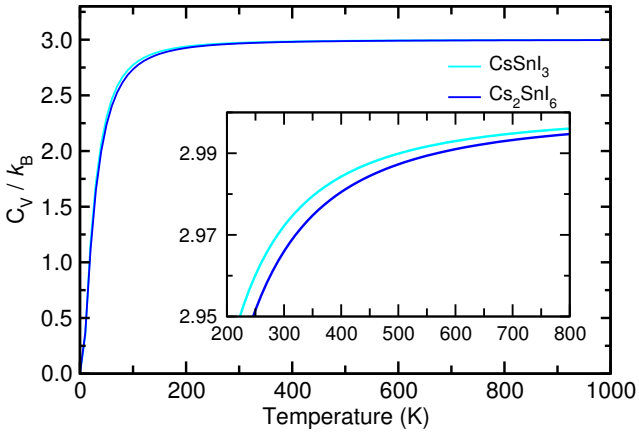

Fig. S8. Heat capacity C_V computed by SCP theory at 500 K for Cs_2SnI_6 and $CsSnI_3$.

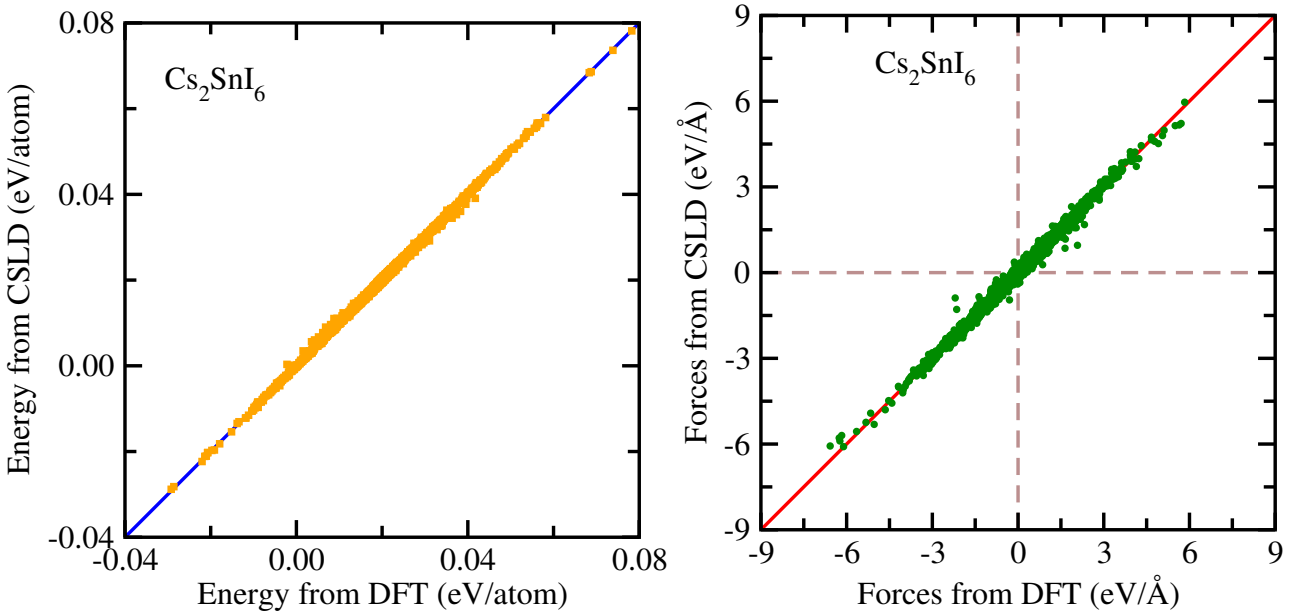

Fig. S9. Comparison of the potential energy and the atomic forces obtained from DFT and IFCs for Cs_2SnI_6.

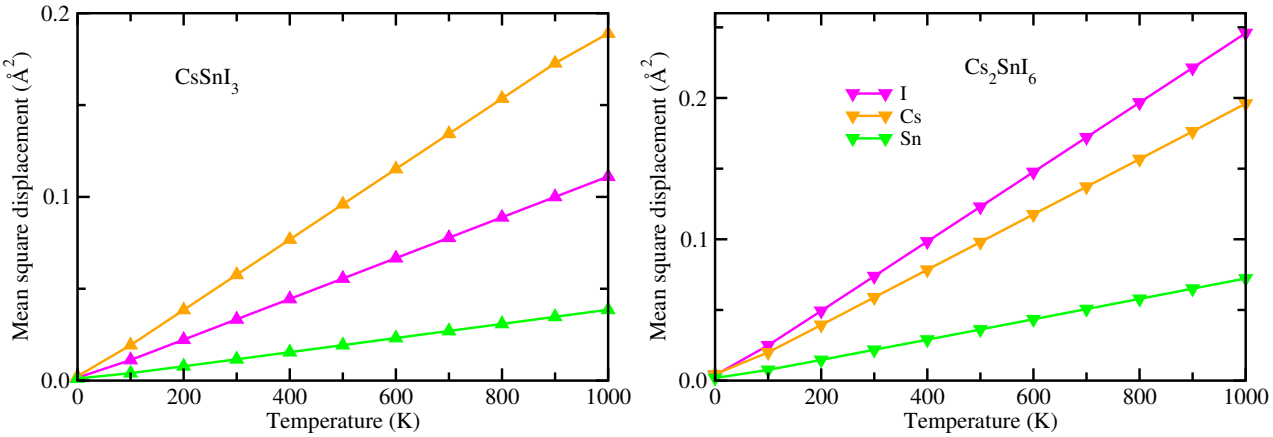

Fig. S10. Mean square displacement as a function of temperature for Cs_2SnI_6 and $CsSnI_3$.

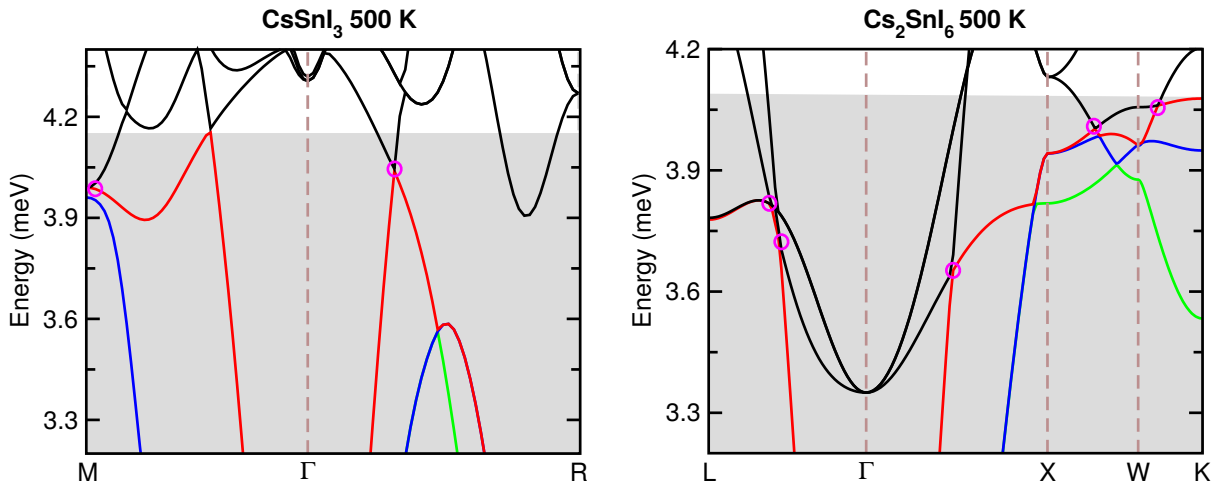

Fig. S11. Phonon dispersion curves near the acoustic phonon region (gray-colored region) around the Γ point obtained by the SCP calculations at 500 K for Cs_2SnI_6 and $CsSnI_3$, respectively. A longitudinal (red) and two transverse acoustic modes (blue and green) are displayed by the colorful solid lines, while low-lying optical modes by black solid lines. The magenta circles represent for the avoided-crossing points between the low-lying optical and longitudinal acoustic modes.

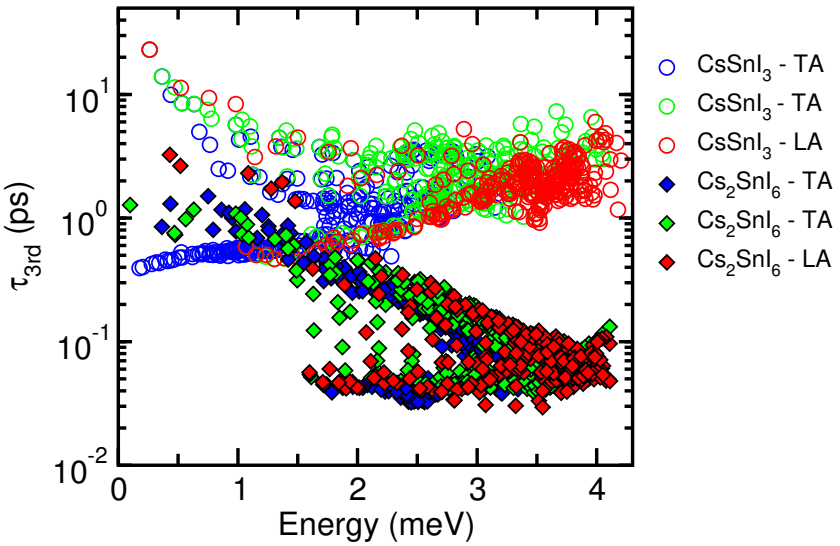

Fig. S12. Phonon lifetime τ_{3rd} projected on the longitudinal (LA, red symbols) and the two transverse acoustic modes (TA, blue and green symbols) at 500 K for Cs_2SnI_6 and $CsSnI_3$, respectively.

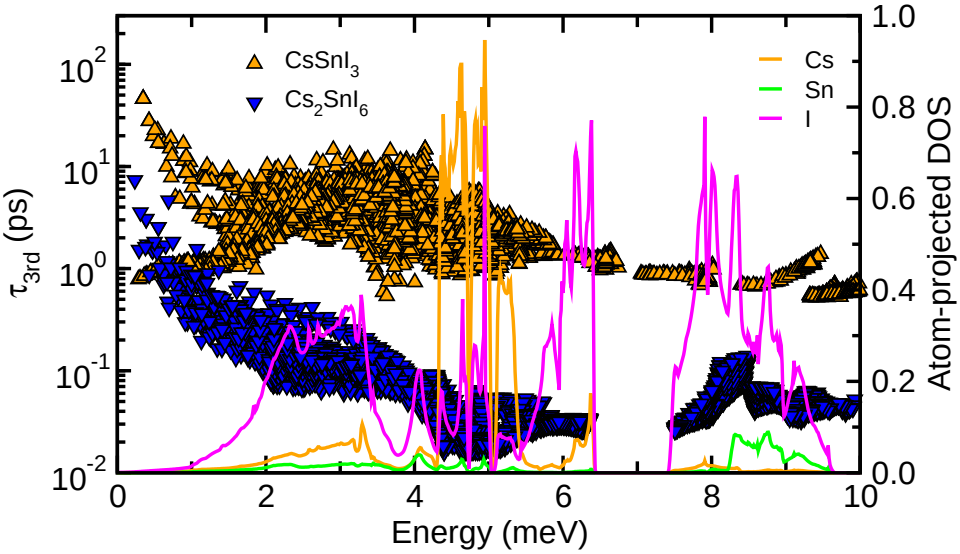

Fig. S13. Phonon lifetime τ_{3rd} of Cs_2SnI_6 and $CsSnI_3$, and atom-projected phonon DOS of Cs_2SnI_6 within the phonon energies from 0 to 10 meV at 500 K.

References

[1] G. Kresse and J. Furthmüller, Effciency of Ab-Initio Total Energy Calculations for Metals and Semiconductors Using a Plane-Wave Basis Set, Comput. Mater. Sci. **6**, 15–50 (1996).

[2] G. Kresse and J. Furthmüller, Efficient Iterative Schemes for Ab Initio Total-Energy Calculations Using a Plane-Wave Basis Set, Phys. Rev. B **54**, 11169–11186 (1996).

[3] P. E. Blöchl Projector Augmented-Wave Method, Phys. Rev. B **50**, 17953–17979, (1994).

[4] G. Kresse and D. Joubert, From Ultrasoft Pseudopotentials to the Projector Augmented-Wave Method, Phys. Rev. B **59**, 1758–1775, (1999).

[5] J. P. Perdew, A. Ruzsinszky, G. I. Csonka, O. A. Vydrov, G. E. Scuseria, L. A. Constantin, X. Zhou, and K. Burke, Restoring the Density Gradient Expansion for Exchange in Solids and Surfaces, Phys. Rev. Lett. **100**, 136406 (2008).

[6] H. Xie, S. Hao, J. Bao, T. J. Slade, G. J. Snyder, C. Wolverton and M. G. Kanatzidis, All-Inorganic Halide Perovskites as Potential Thermoelectric Materials: Dynamic Cation off-Centering Induces Ultralow Thermal Conductivity, J. Am. Chem. Soc. **142**, 9553–9563 (2020).

[7] A. E. Maughan, A. M. Ganose, A. M. Candia, J. T. Granger, D. O. Scanlon and J. R. Neilson, Anharmonicity and Octahedral Tilting in Hybrid Vacancy-Ordered Double Perovskites, Chem. Mater. **30**, 472–483 (2018).

[8] T. Tadano, Y. Gohda and S. Tsuneyuki, Anharmonic Force Constants Extracted from Frst-Principles Molecular Dynamics: Applications to Heat Transfer Simulations, J. Phys.: Condens. Matter. **26**, 225402 (2014).

[9] T. Tadano and S. Tsuneyuki, Self-Consistent Phonon Calculations of Lattice Dynamical Properties in Cubic $SrTiO_3$ with First-Principles Anharmonic Force Constants, Phys. Rev. B **92**, 054301 (2015).

[10] F. Zhou, W. Nielson, Y. Xia, and V. Ozoliņš, Lattice Anharmonicity and Thermal Conductivity from Compressive Sensing of First-Principles Calculations, Phys. Rev. Lett. **113**, 185501 (2014).

[11] M. Simoncelli, N. Marzari, and F. Mauri, Unified Theory of Thermal Transport in Crystals and Glasses, Nat. Phys. **15**, 809–816 (2019).

[12] J. Even, M. Carignanob, and C. Katan, Molecular Disorder and Translation/Rotation Coupling in the Plastic Crystal Phase of Hybrid Perovskites, Nanoscale **8**, 6222 (2016).

[13] U.-G. Jong, C.-J. Yu, Y.-H. Kye, S.-H. Choe, J.-S. Kim, and Y.-G. Choe, Anharmonic Phonons and Phase Transitions in the Vacancy-Ordered Double Perovskite Cs_2SnI_6 from First-Principles Predictions, Phys. Rev. B **99**, 184105 (2019).

[14] Y. Xia and V. Ozoliņš and C. Wolverton, Microscopic Mechanisms of Glass-Like Lattice Thermal Transport in Cubic $Cu_{12}Sb_4S_{13}$ Tetrahedrites, Phys. Rev. Lett. **125**, 085901 (2020)